# Tomographic Reconstruction of Three-Dimensional Volumes Using the Distorted Born Iterative Method

Roberto J. Lavarello*, *Student Member, IEEE*, and Michael L. Oelze, *Senior Member, IEEE*

***Abstract*—Although real imaging problems involve objects that have variations in three dimensions, a majority of work examining inverse scattering methods for ultrasonic tomography considers 2-D imaging problems. Therefore, the study of 3-D inverse scattering methods is necessary for future applications of ultrasonic tomography. In this work, 3-D reconstructions using different arrays of rectangular elements focused on elevation were studied when reconstructing spherical imaging targets by producing a series of 2-D image slices using the 2-D distorted Born iterative method (DBIM). The effects of focal number f/#, speed of sound contrast $\Delta c$, and scatterer size were considered. For comparison, the 3-D wave equation was also inverted using point-like transducers to produce fully 3-D DBIM image reconstructions. In 2-D slicing, blurring in the vertical direction was highly correlated with the transmit/receive elevation point-spread function of the transducers for low $\Delta c$. The eventual appearance of overshoot artifacts in the vertical direction were observed with increasing $\Delta c$. These diffraction-related artifacts were less severe for smaller focal number values and larger spherical target sizes. When using 3-D DBIM, the overshoot artifacts were not observed and spatial resolution was improved. However, results indicate that array configuration in 3-D reconstructions is important for good image reconstruction. Practical arrays were designed and assessed for image reconstruction using 3-D DBIM.**

***Index Terms*—Fully 3-D image reconstruction, inverse scattering, ultrasonic imaging, ultrasonic tomography.**

## I. Introduction

ULTRASONIC computerized tomography (UCT) is an imaging technique that can provide quantitative images of acoustic properties of tissue. UCT has been extensively studied since the early 1970s, which has resulted in the development of several algorithms both from researchers in acoustic and electromagnetic wave propagation [1]–[8]. One of the most well-studied UCT algorithms is inverse scattering using Newton-type methods such as the distorted Born iterative method (DBIM) [9], [10]. One of the drawbacks of this method is that it diverges when the excess phase $\Delta\phi$, which is accumulated by the acoustic wave when traveling through the imaging target, is larger than $\pi$. However, this condition can be avoided using multiple frequency information [11]–[14], which allows the use of inverse scattering for the solution of practical imaging problems. A majority of work examining ultrasonic tomography methods considers 2-D imaging problems. However, real imaging problems involve objects that have variations in three dimensions. Therefore, the study of 3-D inverse scattering methods for image reconstructions is necessary for future applications of ultrasonic tomography.

The most common approach for 3-D inverse scattering imaging consists of using transducers focused on elevation to create a series of 2-D image slices of the object using 2-D DBIM. The resulting 3-D image reconstruction is rendered by stacking the serial 2-D slices. Most current ultrasonic tomography devices [15]–[17] consist of ring arrays focused in elevation, and therefore the effects in the reconstructed profiles due to this particular configuration need to be analyzed.

A more direct approach consists of using 3-D inverse scattering algorithms to reconstruct the imaging target. Unlike the 2-D slicing, point-like transducers are used such that both the transmission and reception beam patterns completely cover the object. With the advent of faster electronics and improved transducer technology, ultrasonic tomography systems with 3-D imaging capabilities are starting to become available [18], [19]. Three-dimensional imaging algorithms have been studied both for the electromagnetic and acoustic case, using Newton-type and conjugate gradient [20]–[22], local shape function [23], propagation–backpropagation [24], and contrast source inversion methods [25]–[27], among others [28], [29].

The main contribution of the present work is to study the performance of 3-D imaging using both 2-D slicing and fully 3-D inverse scattering when reconstructing spherical objects. The simplicity of the imaging targets allows for a straightforward assessment of the reconstruction quality. The performance of 2-D slicing when reconstructing spherical targets with both plane [30] and cylindrical [31] wave illumination and point receivers has already been documented. However, to the authors' knowledge a similar study using nonlinear inverse scattering algorithms and focused transducers is not available in the literature. Given that inverse scattering is a nonlinear problem and therefore imaging target dependent, the effects of focal number f/#, speed of sound contrast $\Delta c$, and scatterer size were considered when using the 2-D DBIM for reconstructing the 2-D slices. In addition, the performance of 3-D DBIM was studied in this work for comparison with the 2-D DBIM and slicing counterpart. To the authors' knowledge, a study about the impact of array configuration in the quality of 3-D acoustic inverse scattering images is not available in the literature. In particular, the effects of transducer placement in the reconstruction quality

Manuscript received April 21, 2009; revised June 14, 2009. First published June 30, 2009; current version published September 25, 2009. This work was supported in part by a grant from the 3M Corporation. *Asterisk indicates corresponding author.*

*R. J. Lavarello is with the Department of Electrical and Computer Engineering, University of Illinois at Urbana-Champaign, Urbana, IL 61801 USA (e-mail: lavarell@illinois.edu).

M. L. Oelze is with the Department of Electrical and Computer Engineering, University of Illinois at Urbana-Champaign, Urbana, IL 61801 USA.

Digital Object Identifier 10.1109/TMI.2009.2026274

were taken into account by testing three different array configurations: a sphere array and two different cylindrical array topologies.

## II. Distorted Born Iterative Method

As in a previous manuscript [14], the details of the distorted Born iterative method [9], [10] are presented here for completeness. The wave propagation in an inhomogeneous medium can be described by the integral equation

$$p(\vec{r}) = p^{\text{inc}}(\vec{r}) + \int_{\Omega} d\vec{r}' \mathcal{O}(\vec{r}') p(\vec{r}') G_0(\vec{r}, \vec{r}') \tag{1}$$

where $p(\vec{r})$ is the acoustic pressure, $p^{\text{inc}}(\vec{r})$ is the incident field, and $G_0(\vec{r}, \vec{r}')$ is the Green's function corresponding to a background with wave number $k_0$. The object function $\mathcal{O}(\vec{r})$ contains the information about the acoustic properties of the imaging target. For the case of constant density and negligible attenuation (see comments at the end of Section V-A), $\mathcal{O} = (k^2(\vec{r}) - k_0^2)$. Equation (1) can be discretized using the method of moments (MoM) and written in matrix form, both for the pressure field inside the computational domain $\bar{p}$ and the scattered field outside the computational domain $\bar{p}^{\text{sc}}$, as

$$\bar{p} = (\bar{I} - \bar{C} \cdot \mathcal{D}(\bar{\mathcal{O}}))^{-1} \cdot \bar{p}^{\text{inc}} \tag{2}$$

$$\bar{p}^{\text{sc}} = \bar{B} \cdot \mathcal{D}(\bar{\mathcal{O}}) \cdot \bar{p} \tag{3}$$

where $\bar{B}$ is a matrix with the Green's coefficients from each pixel to the receivers, $\bar{C}$ is a matrix with the Green's coefficients among all the pixels, and $\mathcal{D}$ is an operator that transforms a vector into a diagonal matrix. The discretization of (1), both for the 2-D and 3-D cases, was performed using sinc basis and delta testing functions [32].

In order to reconstruct the object function from the scattered field data, an iterative algorithm is used. A trial $\bar{\mathcal{O}}_{(0)}$ is chosen for which the corresponding scattered field is calculated. Next, the object function is updated as $\bar{\mathcal{O}}_{(n+1)} = \bar{\mathcal{O}}_{(n)} + \Delta\bar{\mathcal{O}}_{(n)}$, where $\Delta\bar{\mathcal{O}}_{(n)}$ is given by the regularized optimization problem

$$\Delta\bar{\mathcal{O}}_{(n)} = \underset{\Delta\bar{\mathcal{O}}}{\operatorname{argmin}} \left\| \Delta\bar{p}^{\text{sc}} - \bar{F}_{(n)} \cdot \Delta\bar{\mathcal{O}} \right\|_2^2 + \gamma \|\Delta\bar{\mathcal{O}}\|_2^2 \tag{4}$$

where $\Delta\bar{p}^{\text{sc}}$ contains the difference between the predicted and measured scattered fields and $\gamma$ is the regularization parameter. The Frechet derivative matrix $\bar{F}_{(n)}$ has the form [10]

$$\bar{F}_{(n)} = \bar{B} \cdot \left\{ \bar{I} - \mathcal{D}\left(\bar{\mathcal{O}}_{(n)}\right) \cdot \bar{C} \right\}^{-1} \cdot \mathcal{D}(\bar{p}). \tag{5}$$

The iterative process is repeated until the relative residual error (RRE), given by $\text{RRE} = \|\Delta\bar{p}^{\text{sc}}\|_2 / \|\bar{p}^{\text{sc}}\|_2$, falls within a desired termination tolerance. The regularization parameter was chosen using the method described in [33], i.e.,

$$\gamma = 0.5\sigma_0^2 \max\{10^{\log_2 \text{RRE}}, 10^{-4}\} \tag{6}$$

where $\sigma_0^2$ is the square of the dominant singular value of $\bar{F}_{(n)}$ calculated using the power iteration with Rayleigh quotient estimation. All reconstructions in the present work, unless indicated, were terminated when RRE $< 2\%$ and with noiseless simulated data. The accuracy of the reconstructions was quantified by using the mean average error (MAE)

$$\text{MAE} = \frac{\|\Delta\hat{c} - \Delta c\|_1}{\|\Delta c\|_1} \tag{7}$$

where $\Delta\hat{c}$ and $\Delta c$ are the reconstructed and ideal speed of sound contrasts, respectively.

The single frequency DBIM diverges when the magnitude of the excess phase $\Delta\phi$ accumulated by the acoustic wave when traveling through the scatterer approaches $\pi$ [34]. For a homogeneous sphere, $\Delta\phi$ can be estimated as

$$\Delta\phi = 2k_0 a \left(c_r^{-1} - 1\right) \tag{8}$$

where the relative speed of sound $c_r = c/c_0$ and $a$ is the sphere radius. When using the linearized first-order Born approximation, the reconstructions degrade for even smaller $|\Delta\phi|$ values [35]. Therefore, any scatterer with $|\Delta\phi| > \pi$ will be considered to exhibit a large acoustic contrast in the present work.

## III. 3-D Reconstructions by Slicing Using Focused Transducers

### A. Data Generation

The scattered data for each slice were generated using (3) with the computational domain discretized using cubic pixels of size $\lambda/10$, where $\lambda = 2\pi/k_0$. The accuracy of the numerically calculated scattered data is a key factor when assessing the validity of the reconstructions using the focused array. Therefore, the quality of the data generated by the MoM solver was analyzed by calculating the scattering of a Bessel beam by a sphere, for which the exact analytical scattering solution is available in the literature [36]. This particular problem allows the validation of both the ability of the numerical solver to deal with incident fields for which the beamwidth is smaller than the imaging target, and the choice of pixel size for data generation.

The incident field for a Bessel beam of zeroth-order propagating in the $z$ direction is given by

$$p^{\text{inc}}(\vec{r}) = J_0(k_\rho \rho) \exp(-jk_z z) \tag{9}$$

where $J_0(x)$ is the zeroth-order Bessel function, $\rho = \sqrt{x^2 + y^2}$, and $k_z$ and $k_\rho$ are the axial and radial wave numbers which satisfy $k_\rho^2 + k_z^2 = k_0^2$. The scattering of a beam with $k_\rho = k_0/6$ (−6-dB beamwidth $\approx 2.9\lambda$) caused by a sphere with radius $a = 4\lambda$ and $c_r = 1.1$ was calculated. The results are shown in Fig. 1. The properties of the sphere were chosen so that $\Delta\phi$ was comparable to the largest values obtained in the following sections. The total acoustic field inside the computational domain had a root mean square error (RMSE) of 0.56% when compared to the analytical solution. Even further, the RMSE between the MoM and analytical scattered fields was only 0.3%. These results indicate that the numerical solver is capable of generating accurate scattered data with beam incident fields.

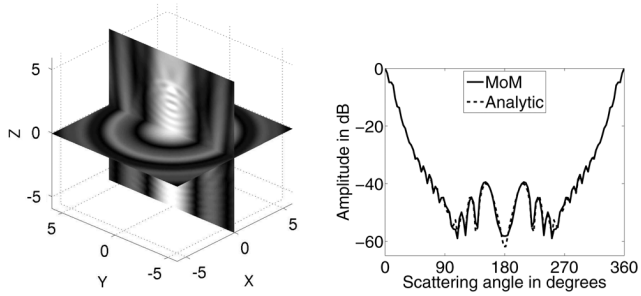


Fig. 1. Scattering of a Bessel beam by a circular cylinder of radius $4\lambda$. Left: pressure field inside the computational domain calculated with the MoM solver. All distances are in units of $\lambda$. Right: scattered pressure values as a function of the scattering angle measured away from the Z axis on the XZ plane. Both the MoM field (solid line) and the analytic solution to the scattering problem (dashed line) are shown.

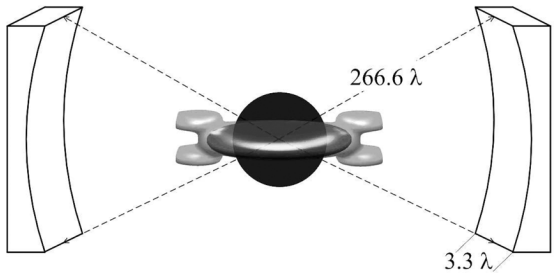


Fig. 2. Schematic of the transducer placement used for 2-D DBIM and slicing imaging. The imaging target (dark volume) is placed within the overlap of the focal zones of the transducers (gray volumes). The transducers are focused only on elevation. Only two transducers are shown for simplicity.

### B. Simulated Array Configuration

The simulated imaging system consisted of a ring array with 110 rectangular elements focused in elevation. Each element had a width of $3.3\lambda$ and a focal distance of $266.6\lambda$. The focal number $(f/\#)$ was changed by modifying the height of the elements. Different slices were calculated by introducing a vertical offset between the transducers and the imaging target. A schematic of the imaging configuration is shown in Fig. 2.

Both the incident field $p^{\text{inc}}(\vec{r})$ and $G_0(\vec{r},\vec{r}')$ were numerically calculated by dividing the array elements into small rectangular subapertures and summing their far field radiation patterns [37]. Focusing was accomplished by introducing phase delays to the rectangular subapertures as a function of their vertical coordinate.

### C. Data Inversion and Results

In linear imaging modalities, such as X-ray tomography, the effect of the finite slice thickness is the introduction of vertical blurring which can be expressed as a convolution

$$\hat{\mathcal{O}}(x,y,z) = \mathcal{O}(x,y,z) * h(z) \tag{10}$$

where $\hat{\mathcal{O}}(x,y,z)$ and $\mathcal{O}(x,y,z)$ are the reconstructed and ideal object function profiles, and $h(z)$ is the vertical point spread function (PSF) of the imaging system. Deconvolution [38], [39] and blind deconvolution [40], [41] techniques have been proposed in other tomographic modalities to reduce the blurring effect. Given that the geometric focal depth is large compared to the dimensions of the imaging targets tested in this work, $|h(z)|$ is approximately proportional to transmit/receive transducer PSF at the focal depth, i.e.,

$$|h(z)| \propto \text{sinc}^2\left(\frac{z}{\lambda f/\#}\right) \tag{11}$$

where $\text{sinc}(x) = \sin(\pi x)/\pi x$. However, acoustic wave scattering is a nonlinear problem and therefore results will not necessarily correlate with linear imaging predictions, especially when significant multiple scattering is developed.

The reconstruction for each slice was performed using the 2-D DBIM algorithm with both $p^{\text{inc}}(\vec{r})$ and $G_0(\vec{r},\vec{r}')$ proportional to $H_0^{(2)}(\vec{r})$, the Hankel function of the second kind. The computational domain per slice was divided into pixels of size $\lambda/5$, which has been observed to provide accurate 2-D DBIM reconstructions of $\Delta c$ both with simulated and experimental data [14]. The vertical spacing between reconstructed slices was set to $\lambda/5$. To obtain a continuous reconstruction in the vertical direction, the reconstruction at the $k$th slice was performed using the reconstruction at the adjacent $(k-1)$th slice as initial guess.

The performance of the 2-D DBIM and slicing algorithm was studied by reconstructing homogeneous spheres of different sizes and speed of sound contrasts. The scattered data per slice were simulated with one transducer acting as a source and the 110 elements acting as receivers. A full dataset of $110\times110$ scattered pressure values per slice was obtained by exploiting symmetries of the imaging targets.

*1) Effects of Focal Number and Speed of Sound Contrast:* Spheres of radius $4\lambda$ and speed of sound contrasts $\Delta c = (c_r - 1)$ of 3%, 6%, and 9% were reconstructed using 2-D DBIM and slicing. The objects were reconstructed using transducers with $f/\#$ values equal to 2, 3, and 4. The reconstructed profiles along the vertical direction are shown in Fig. 3. All plots show the ideal profile, DBIM reconstruction, and the blurred profile predicted by linear theory using (10).

For low speed of sound contrast values ($\Delta c = 3\%$ for which $\Delta\phi = 0.47\pi$) the reconstructed DBIM profile was highly correlated with linear theory predictions for all tested $f/\#$s, as observed in the first column of Fig. 3. The MAE along the vertical line passing through the origin between the reconstructions and the predictions from linear theory are 4.9%, 5.1%, and 5.9% for the $f/2$, $f/3$, and $f/4$ transducers, respectively. Also, and as expected from (10) and (11), the blurring is more severe when using larger $f/\#$ values. The volumetric MAE values between the DBIM reconstructions and the ideal $\Delta c$ distribution were 25.7%, 34.3%, and 42.3% for $f/\#$ values of 2, 3, and 4, respectively.

For moderate $\Delta c$ values ($\Delta c = 6\%$ for which $\Delta\phi = 0.91\pi$), nonlinearities in the wave equation are manifested by an increase in the slope at the edges of the reconstructed profile when compared to the predicted profile, as evidenced in the second column of Fig. 3. This effect was found to be more severe for larger $f/\#$ values. The volumetric MAE values between the DBIM reconstructions and the ideal $\Delta c$ distribution were 23.3%, 29.8%, and 36.0% for $f/\#$ values of 2, 3, and 4, respectively.

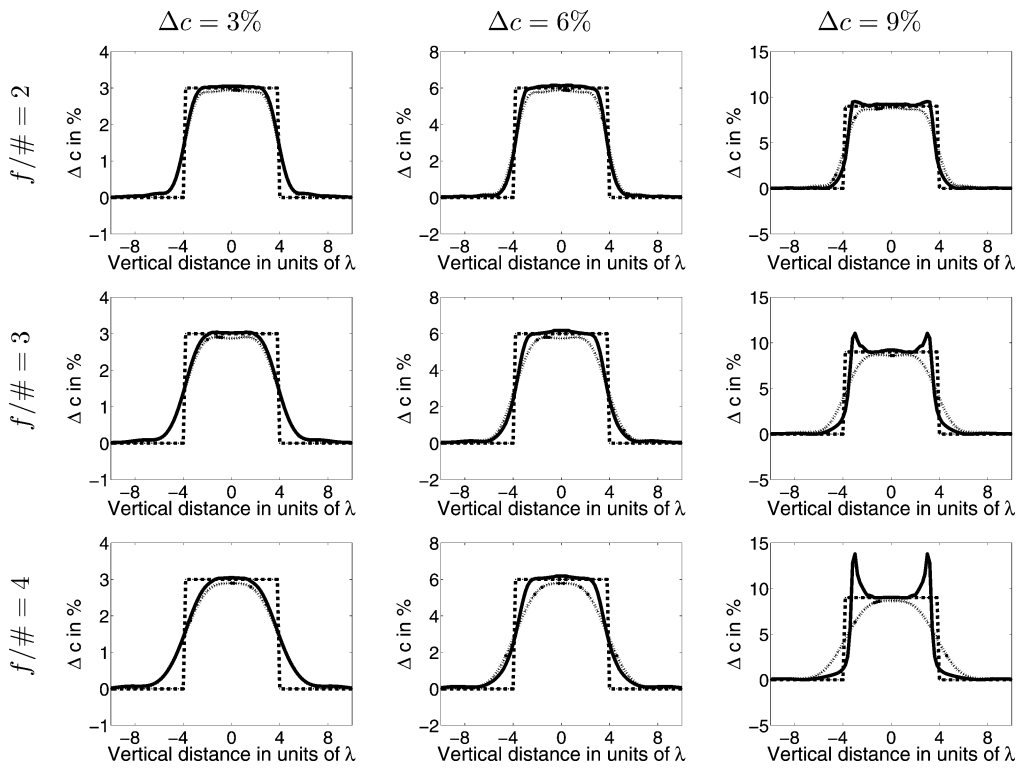


Fig. 3. Reconstructed vertical profiles of a $4\lambda$ radius sphere for speed of sound contrasts of 3% (first column), 6% (second column), and 9% (third column), respectively. Top row: f/2 transducers. Center row: f/3 transducers. Bottom row: f/4 transducers. All plots show the ideal profile (dashed line), the DBIM profile (solid line), and the profile predicted using linear convolution (dotted line).

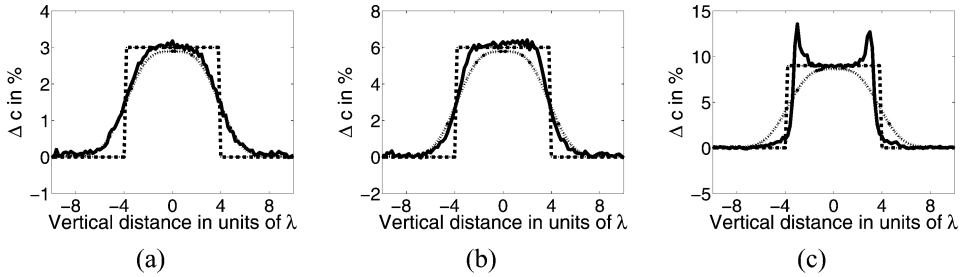


Fig. 4. Reconstructions of spheres of radius $4\lambda$ using f/4 transducers and noisy data. The speed of sound contrast was set to (a) 3%, (b) 6%, and (c) 9%. All plots show the ideal profile (dashed line), the DBIM profile (solid line), and the profile predicted using linear convolution (dotted line).

The most significant effect was found for even larger values of speed of sound contrast, for which a significant amount of multiple scattering was developed ($\Delta c = 9\%$ for which $\Delta\phi = 1.32\pi$). Overshoots can be observed at the edges of the reconstructed profiles (third column of Fig. 3). The magnitude of the overshoots was more significant for larger $f/\#$ values. The volumetric MAE values between the DBIM reconstructions and the ideal $\Delta c$ distribution were 21.4%, 25.9%, and 32.4% for $f/\#$ values of 2, 3, and 4, respectively. The overshoot amplitudes were 6.0%, 22.7%, and 53.2% above the intended $\Delta c$ values for $f/\#$ values of 2, 3, and 4, respectively.

In order to validate the performance of 2-D DBIM and slicing in the presence of noise, the inversions were also carried out with noisy data. The scattered data were contaminated using 2% Gaussian noise. Typical results are shown in Fig. 4. The regularization approach resulted in reconstructions that were virtually unaffected by noise. Therefore, noiseless data will be used for the remainder of this work.

*2) Effects of DBIM Initial Guess:* It may be argued that the artifacts are due to the choice of initial guess when performing the 2-D DBIM inversions. In order to test this, reconstructions were also obtained using two different initialization approaches for the 2-D DBIM algorithm. For the first approach, 90% of the ideal object function was used as initial guess. For the second approach, frequency hopping [11] using an auxiliary frequency of $f_0/2$ was used. For illustration, the reconstructed profiles in the vertical direction of the $\Delta c = 9\%$ sphere using all three initialization procedures and f/4 transducers are shown in Fig. 5. The overshoot artifacts were observed for all cases, and therefore were not caused by the choice of initial guess but were instead related to diffracion effects on the measured scattered field that could not be properly compensated for using 2-D imaging algorithms.

*3) Effects of Scatterer Radii:* It is also of interest to study the performance of 2-D DBIM and slicing when larger scatterers are imaged. Therefore, spheres of diameters $12\lambda$ and $16\lambda$ were also

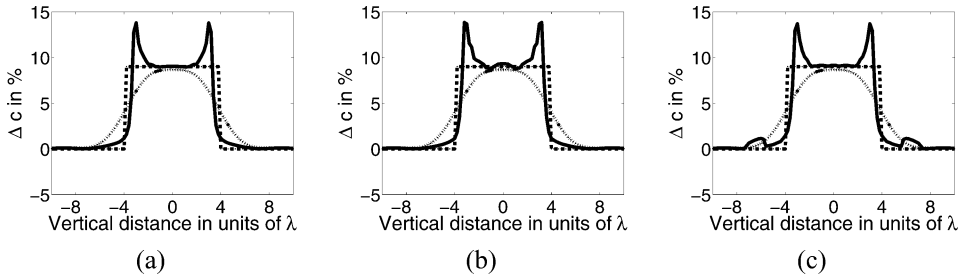


Fig. 5. Reconstructions of a sphere of radius $4\lambda$ and $\Delta c = 9\%$ using three different initialization approaches. (a) Initial guess chosen as the previous slice reconstructed. (b) Initial guess chosen as 90% of the ideal object function. (c) Frequency hopping with frequencies $f_0/2$ and $f_0$. All plots show the ideal profile (dashed line), the DBIM profile (solid line), and the profile predicted using linear convolution (dotted line).

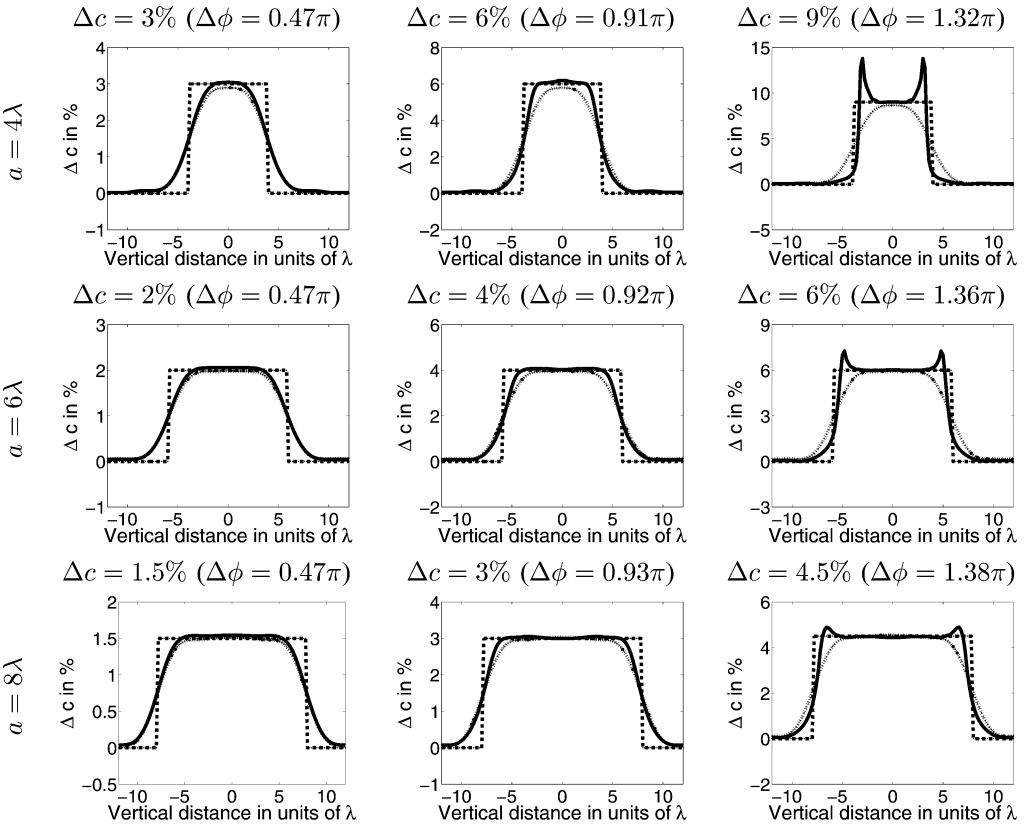


Fig. 6. Reconstructed vertical profiles of spheres for speed of sound contrasts of $(4\lambda/a)$ 3% (first column), $(4\lambda/a)$ 6% (second column), and $(4\lambda/a)$ 9% (third column), respectively, using $f/4$ transducers. Top row: $a = 4\lambda$. Center row: $a = 6\lambda$. Bottom row: $a = 8\lambda$. All plots show the ideal profile (dashed line), the DBIM profile (solid line), and the profile predicted using linear convolution (dotted line).

reconstructed for three different $\Delta c$ values. As the scatterer size increases, the amount of multiple scattering for a fixed speed of sound contrast $\Delta c$ also increases. In order to facilitate the comparison among different imaging targets, spheres with three excess phase $\Delta\phi$ values ($\Delta\phi$ of approximately $0.47\pi$, $0.92\pi$, and $1.35\pi$) were reconstructed. The $\Delta\phi$ values were obtained by setting the speed of sound contrast values to $(4\lambda/a)$ 3%, $(4\lambda/a)$ 6%, and $(4\lambda/a)$ 9%. With these $\Delta c$ values, the differences between the intended and actual $\Delta\phi$ values were of less than 3%. The results are shown in Fig. 6.

Even though the overshoot artifacts were present for all sphere sizes, their amplitudes were smaller when imaging larger targets with similar $\Delta\phi$ values. This is to be expected because if the sphere radius increases, relative geometrical variations in the vertical direction are reduced throughout the extent of the $-6$-dB vertical beamwidth if the transducer $f/\#$ is kept constant. Therefore sections of the sphere within a vertical beamwidth appear more cylindrical, which makes the 2-D approximation more accurate and in turn reduces the artifacts in the 3-D reconstruction.

## IV. 3-D DBIM Using Point-Like Transducers

The results from Section III indicate that not taking vertical diffraction into account may result in reconstructions with severe distortions. Diffraction in all directions can be compensated for by inverting the 3-D wave equation using 3-D DBIM. Unlike the 2-D DBIM and slicing approach, distributions of point-like transducers are used to collect the scattered data. For proper sampling of the scattered data, uniform angular spacing

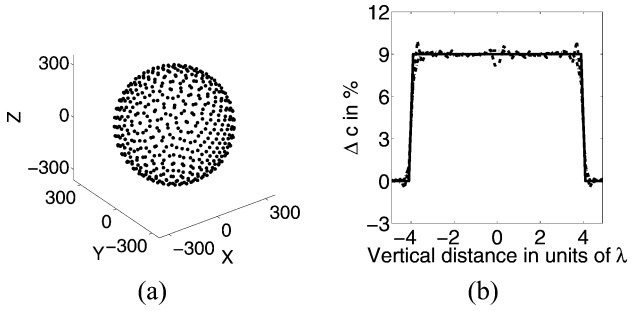


Fig. 7. (a) Transducer distribution of a sphere array (dimensions in units of $\lambda$) with $N_t = 450$. (b) Reconstructed vertical profile of a sphere of radius $4\lambda$ and $\Delta c = 9\%$ using the sphere array. Solid line: ideal profile. Dashed line: reconstructed profile. Dotted line: reconstructed profile with median filtering.

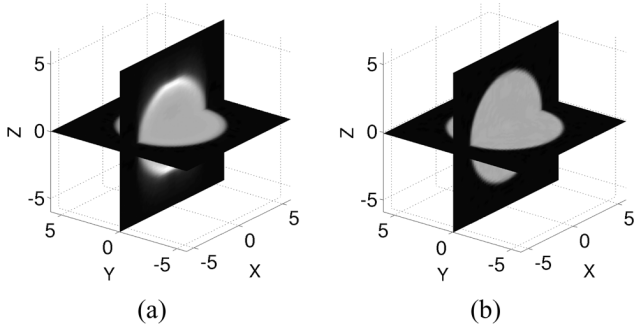


Fig. 8. Reconstructions of a sphere of radius $4\lambda$ and $\Delta c = 9\%$ using (a) 2-D slicing with $f/4$ transducers, and (b) 3-D DBIM with a sphere array. All dimensions are in units of $\lambda$.

between adjacent transducers is commonly used in acoustic tomography. For the 2-D case, such arrangement corresponds to placing the transducers uniformly over a circular arc [14]. For the 3-D imaging case, several arrangements have been proposed since the developments of linearized inversion algorithms [42]. In this work, two kinds of arrays (spherical and cylindrical arrays) were studied when reconstructing sphere targets using 3-D DBIM.

### A. 3-D DBIM With a Sphere Array

The more direct 3-D extension of the circular array configuration for 2-D imaging is to distribute the transducers uniformly over a spherical surface. This problem is commonly solved using optimization routines [43]. In this work, a highly uniform distribution of $N_t$ point-like transducers over a spherical surface of radius $R$ was obtained by using a Coulomb energy minimization algorithm [44]. This approach consists of minimizing the energy function

$$E_C(N) = \sum_{i=1}^{N_t} \sum_{j>i}^{N_t} \frac{1}{|\vec{r}_i - \vec{r}_j|} \tag{12}$$

where $\vec{r}_i$ represents the location of the $i$th transducer. The minimization is performed with the constraint of $|\vec{r}_i| = R, \forall i \in [1, N_t]$.

For comparison with the results presented in Section III-C1, spheres of radius $4\lambda$ and $\Delta c$ values of 3%, 6%, and 9% were reconstructed using 3-D DBIM. The scattered data was generated by adapting the analytic solution of the scattering of a plane wave by a sphere [45]. The computational region was discretized using $50 \times 50 \times 50$ pixels of size $\lambda/5$. A sphere array with $R = 300\lambda$ and $N_t = 450$ [shown in Fig. 7(a)] was simulated, which provided an overdetermination factor (i.e., the ratio between the number of simulated data points and the number of unknowns) of approximately 1.6. Frequency hopping with an auxiliary frequency of $f_0/2$ and a $25 \times 25 \times 25$ grid was used so that convergence could be achieved for all analyzed cases. The reconstruction MAE were equal to 12.2%, 12.4%, and 11.8% for $\Delta c$ values of 3%, 6%, and 9%, respectively. For illustration, the vertical profile of the 3-D DBIM reconstruction corresponding to $\Delta c = 9\%$ is shown in Fig. 7(b). A conventional median filter [46] was used to smooth out the reconstructed profile.

The volumetric reconstructions of a sphere of radius $4\lambda$ and $\Delta c = 9\%$ using both 2-D DBIM and slicing with the $f/4$ array and 3-D DBIM with the sphere array are shown in Fig. 8. For the 2-D case, the diffraction effects are more severe when the portion of the imaging target intersected by the effective transducer slice exhibits a larger vertical variation. As a result, vertical slices closer to the top and bottom of the sphere appear more distorted than the ones closer to the center. When using the full 3-D approach, the spatial resolution is comparable in all directions and no overshoot artifacts or excessive vertical blurring are observed.

### B. 3-D DBIM With a Cylinder Array

Even though the sphere array yields accurate 3-D DBIM reconstructions, other array configurations may either be simpler to construct or allow for easier imaging target placement. One of those geometries consists of using a cylinder array with transducers arranged in $N_r$ circular rings with $N_a$ transducers per ring [19]. In this case, the object to be imaged may be easily placed in the bore of the cylindrical array for easier access than a spherical array configuration.

The elevation angle $\theta$ of each ring was distributed uniformly within a range $\Delta\theta$ centered around $\theta = 90°$ (corresponding to the XY plane). The azimuthal angle $\phi$ of each transducer within a ring was uniformly distributed between 0° and 360°. The transducers were arranged in vertical columns, as shown in Fig. 9(a). A simple variation consists of introducing an angular shift $\phi'$ between consecutive rings in order to obtain more data diversity, which is illustrated in Fig. 9(b). For the present work, the angular shift was chosen to be $\phi' = (\pi)/(2N_r)$.

The quality of data diversity obtained with a particular sampling configuration is difficult to analyze for the full wave equation case, but is a well understood problem if multiple scattering can be neglected. Under this assumption, the Fourier diffraction theorem [47], [48] states that if the transmitted field has an incident direction given by $\vec{u}_t$, measurements of the scattering pattern at directions $\vec{u}_s$ will provide information of the 3-D Fourier transform of the imaging target at the $k$-space vectors

$$\vec{K} = k_0(\vec{u}_s - \vec{u}_t). \tag{13}$$

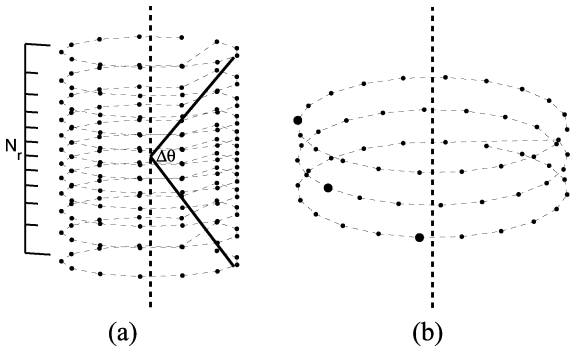


Fig. 9. Geometry of two cylinder array configurations. (a) Cylindrical array with the transducers arranged in columns (no angular shifting). The transducers are arranged in $N_r$ rings that span an elevation angle range $\Delta\theta$ around the XY plane. (b) Cylindrical array with angular shifting between adjacent rings. The large dot marks correspond to the locus of the first transducer for each ring.

For illustration, scatter plots of the *k*-space coverage as predicted by the Fourier diffraction theorem corresponding to some sphere ($N_t = 450$) and cylinder ($N_r = 22$ and $N_a = 20$) array configurations are shown in Fig. 10. For simplicity in visualization the projections in the $k_x - k_y$ and $k_x - k_z$ planes of only the vectors for which $|k_z/k_0| < 0.1$ and $|k_y/k_0| < 0.1$, respectively, are displayed. Reconstructions of a sphere of radius $4\lambda$ and $\Delta c = 6.4\%$ using each array are also shown. It is not intended here to suggest that diffraction tomography theory is a valid approach to reconstruct such a scatterer, and therefore the *k*-space coverage plots are shown only with the intent of understanding the quality of the scattered field sampling.

As observed on the first row of Fig. 10, when using the sphere array the *k*-space coverage was very uniform in every direction and the chosen imaging target was properly reconstructed ($\mathrm{MAE} = 13.8\%$). When using cylinder arrays with angular shift (second and fourth rows of Fig. 10 for $\Delta\theta = 140°$ and $\Delta\theta = 80°$, respectively) the *k*-space coverage was relatively uniform, although some clustering was observed especially at high frequencies on the $k_x - k_y$ plane. The reconstructions exhibited good accuracy ($\mathrm{MAE} = 14.3\%$ for $\Delta\theta = 140°$ and $\mathrm{MAE} = 12.6\%$ for $\Delta\theta = 80°$), with some blurring introduced for reduced $\Delta\theta$ values as a consequence of the reduced *k*-space coverage in the vertical direction. In contrast, the *k*-space coverage when using the cylinder array without angular shift (third and fifth rows of Fig. 10 for $\Delta\theta = 140°$ and $\Delta\theta = 80°$, respectively) exhibited a more significant amount of clustering when compared to the other configurations, especially when using reduced $\Delta\theta$ values. Even for relatively high $\Delta\theta$ values, the reconstructed 3-D DBIM profiles were somewhat distorted ($\mathrm{MAE} = 17.5\%$ for $\Delta\theta = 140°$). The quality of the reconstructions degraded dramatically as $\Delta\theta$ was further reduced. When using $\Delta\theta = 80°$, the reconstruction lacked both quantitative and qualitative value. Even further, the reconstruction error ($\mathrm{MAE} = 47.6\%$) was nearly 2.8 times larger than the one obtained with the equivalent array using angular shifting. Therefore, angular shifting among rings resulted in improved *k*-space sampling with no additional complications on the array manufacturing process when compared to the array with no shifting.

Even with the use of angular shifting, special care must be taken when constructing a cylinder array in order to have an adequate *k*-space sampling. The performance of the cylinder array was briefly studied using two quality metrics.

1) The spatial resolution as measured by the $\mathrm{MTF}_{-20\,\mathrm{dB}}$ spatial frequency (i.e., the spatial frequency at which the modulation transfer function drops by a factor of 20 dB). The target for the estimation of the $\mathrm{MTF}_{-20\,\mathrm{dB}}$ was a sphere of radius $\lambda/10$ and $\Delta c = 10\%$. Equation (13) can be used to predict the maximum *k*-space coverage in the vertical direction,

$$k_z^{\max} = 2k_0 \sin(\Delta\theta/2). \tag{14}$$

   For the weakly scattering target used, it was assumed that $\mathrm{MTF}_{-20\,\mathrm{dB}} \approx k_z^{\max}$. For illustration, the results when $N_r/N_a = 1.1$ are shown in Fig. 11(a), both as measured from the simulation reconstructions and as predicted using (14). As expected, the best resolution ($\approx \lambda/4$) is obtained when the angular coverage is closer to the maximum value of 180°. At the point where the angular coverage drops to 60°, the spatial resolution drops by almost a factor of $2(\approx \lambda/2)$.
2) The numerical accuracy as measured by the MAE. Several simulations were conducted to reconstruct a sphere of radius $4\lambda$ and $\Delta c = 6.4\%$ using cylinder arrays with different $\Delta\theta$ and $N_r/N_a$ values, while fixing $N_t = 450$. The results presented in Fig. 11(b) indicate that, even though (14) indicates that larger $\Delta\theta$ are preferred in order to improve spatial resolution, the numerical accuracy of the reconstructions may be compromised if $N_r/N_a$ is not sufficiently large (i.e., an excessive vertical separation between adjacent rings) due to improper sampling of the target's scattering pattern.

## V. Discussion

This work was intended as a fundamental study of the limitations of two approaches for 3-D acoustic inverse scattering imaging. Even though the chosen imaging targets (i.e., homogeneous spheres embedded in a homogeneous background) are not representative of typical medical ultrasonic tomography applications such as breast imaging, important results relevant to 3-D imaging using both 2-D DBIM and 3-D DBIM were obtained.

### A. 2-D DBIM and Slicing Approach

When using 2-D DBIM and slicing, loss of spatial resolution and the eventual appearance of overshoot artifacts in the vertical direction as the speed of sound contrast increased were observed. Both distortions were reduced when using smaller focal numbers. However, the extent of the depth of field $D_z$ for a focused rectangular aperture is approximately given by $D_z = 4\lambda(f/\#)^2$ [49]. Therefore, using small $f/\#$s severely reduces the size of the recoverable imaging targets. As an example, a female breast in the low MHz range will have a size of approximately $100\lambda$, and therefore $f/\# \geq 5$ would be required.

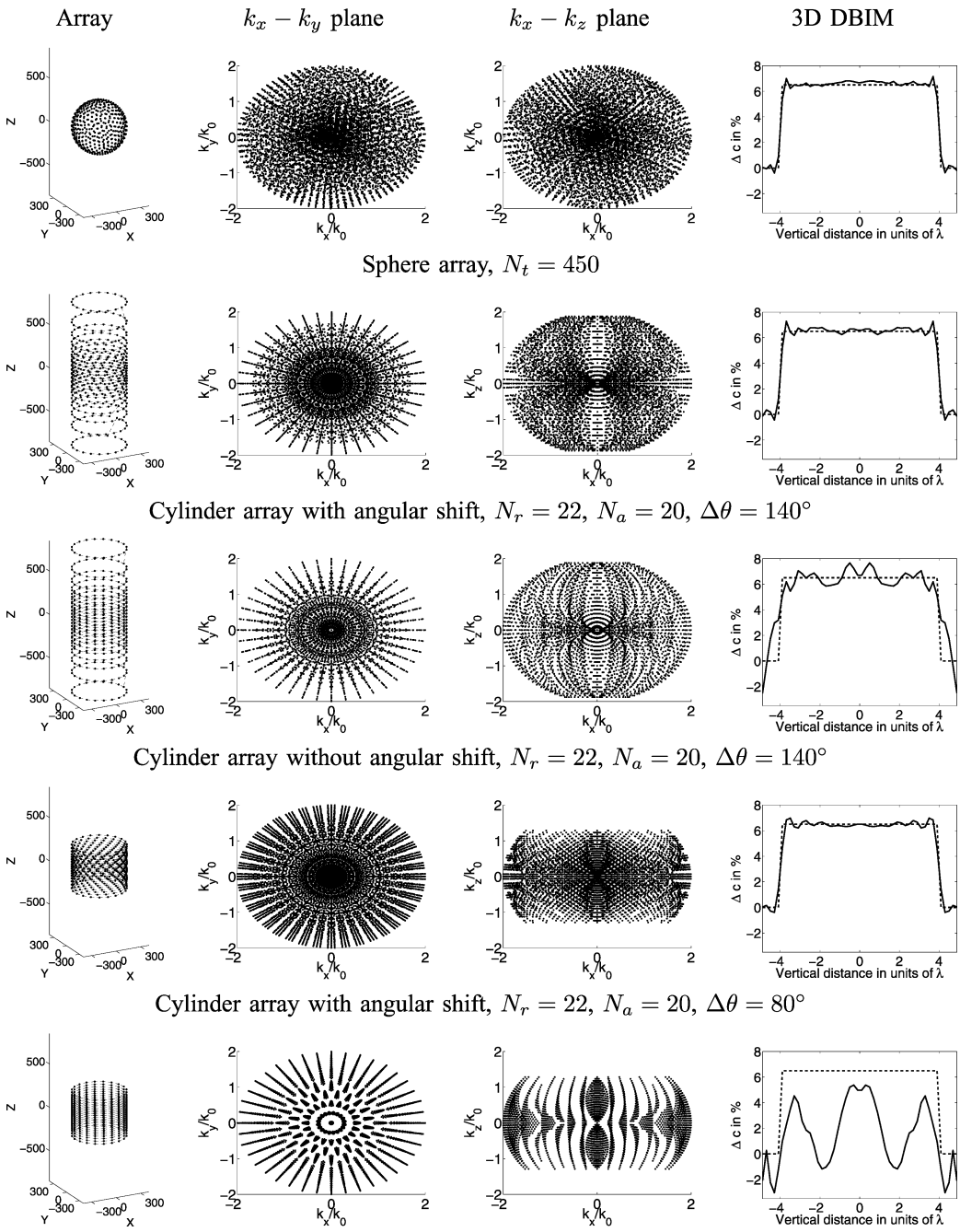


Fig. 10. Different array configurations for 3-D DBIM imaging. For all configurations, the transducer distribution (first column), the *k*-space distribution on the $k_x - k_y$ (second column) and $k_x - k_z$ (third column) planes using the Fourier diffraction theorem, and the reconstruction of a sphere of radius $4\lambda$ and $\Delta c = 6.4\%$ (fourth column) are shown. First row: sphere array with $N_t = 450$. Second row: cylinder array with angular shift, $N_r = 22$, $N_a = 20$, $\Delta\theta = 140°$. Third row: cylinder array without angular shift, $N_r = 22$, $N_a = 20$, $\Delta\theta = 140°$. Fourth row: cylinder array with angular shift, $N_r = 22$, $N_a = 20$, $\Delta\theta = 80°$. Fifth row: cylinder array without angular shift, $N_r = 22$, $N_a = 20$, $\Delta\theta = 80°$.

An important issue is to consider if the artifacts reported in this work should be expected to occur in the context of medical imaging. The most commonly proposed application of ultrasonic tomography is breast imaging. *In vitro* measurements reported by Yang *et al.* [50] corresponding to patients with infiltrating adenocarcinoma and scirrhous duct cell carcinoma indicated that the mean sound speed in the tumors and surrounding media were around 1565 m/s and 1422 m/s, respectively. Measurements of properties of biopsy specimens by Edmons *et al.* [51] indicated speed of sound values ranging between 1400 and 1600 m/s when considering normal (excluding fat), benign, and malignant tissues. When using inverse scattering imaging, Johnson *et al.* [52] reported speed of sound values of benign and malignant inclusions ranging between 1450 m/s and 1600 m/s *in vivo*. Li *et al.* [53] reported mean speed of sound values (considering the whole breast) of 1440 m/s and 1505 m/s for fatty and dense breasts *in vivo* using refraction-corrected ultrasonic tomography. All these results

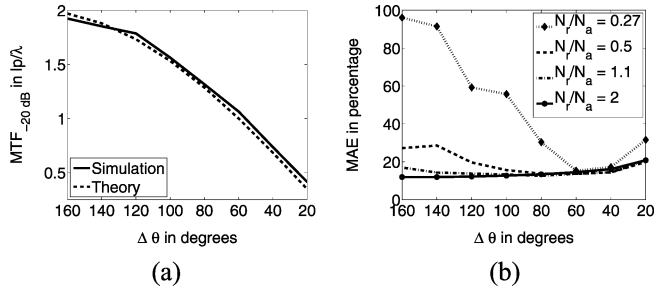


Fig. 11. Performance of the cylinder array with angular shifting as a function of $\Delta\theta$, as measured by (a) the $\text{MTF}_{10}$ when reconstructing a sphere of radius $\lambda/10$ and $\Delta c = 10\%$ and (b) the volumetric MAE when reconstructing a sphere of radius $4\lambda$ and $\Delta c = 6.4\%$.

indicate that relatively large $\Delta c$ values may be found when imaging soft tissues. Using the numbers reported in [50], a speed of sound contrast of 10% (relative to the fatty tissue background) could be expected when imaging a female breast. These values are sufficiently large to potentially generate distortions due to excessive vertical diffraction.

Finally, the results of this study were derived assuming negligible changes in mass density. However, it has been observed in recent studies [14], [33] that speed of sound reconstructions are affected locally in regions of density variations. These effects could even further degrade the quality of 3-D reconstructions using 2-D DBIM and slicing in regions of large vertical variations, e.g., the top and bottom of the spherical targets presented in this study.

### *B. 3-D DBIM Approach*

3-D DBIM was also explored in the present work. Unlike the 2-D DBIM and slicing approach, 3-D DBIM takes into account diffraction in the vertical direction. As expected, the reconstructed profiles are free of artifacts in the vertical direction and do not suffer from excessive blurring in any direction when the transducers are properly distributed. The effects of transducer placement were illustrated through a brief exploration of three different array configurations. The cylinder array without angular shift is a clear example of how a uniform transducer distribution may yield poor results due to high correlation in the measurements.

However, 3-D DBIM is far more computationally intensive than the 2-D slicing counterpart. Here it will be assumed that all $N_t$ transducers are used for transmission and reception, and that the computational domain is discretized using $N$ pixels per dimension. For the 3-D DBIM algorithm, $N_t \propto N^{1.5}$ and memory in the order of $\mathcal{O}(N^{4.5})$ is needed in order to store both the total pressure fields and the Green's function vectors for each DBIM iteration without resorting to disk storage. In contrast, for the 2-D DBIM algorithm $N_t \propto N$ and only one slice ($N^2$ pixels per slice) is processed at a time. Therefore, the memory requirement of 2-D DBIM is in the order of $\mathcal{O}(N^3)$. A more important issue is the execution time of the DBIM algorithm, which is asymptotically dominated for large $N$ values by the matrix-vector multiplications in both (3) and the iterative solution of (4). These operations are of order $\mathcal{O}(N^6)$ ($N_t^2 \times N^3$, with $N_t \propto N^{1.5}$) for the 3-D DBIM approach, but only of order $\mathcal{O}(N^5)$ ($N_t^2 \times N^2$ for all $N$ slices, with $N_t \propto N$) for the 2-D DBIM and slicing approach. These limitations may be overcome by using parallel matrix-free implementations of DBIM, which have effectively relaxed the computing requirements of this algorithm by reducing both the amount of memory and execution time per node [54].

Although the computational complexity of the algorithm increases with the number of transducers used to collect the measurements, large datasets are required to have an over-determined system of equations so that the measurements convey all the information needed to obtain meaningful speed of sound estimates. Recent studies on compressed sensing [55] have indicated that reduced datasets can also provide highly accurate results when reconstructing medical images [56]–[58], but the required algorithms are usually more complex and therefore a reduction in computational complexity may not necessarily follow. Further, for current applications of ultrasonic tomography, scanners capable of collecting up to 80 sets of 2-D data using 256 elements for both transmission and reception in only one minute are currently available [59]. Therefore, the potential of sparse array technology [60] to alleviate some of the limitations of fully 3-D acoustic tomography imaging remains to be determined.

## VI. Conclusion

Two approaches for 3-D inverse scattering reconstructions of speed of sound were studied. When using 2-D DBIM and slicing, artifacts due to large multiple scattering were identified in addition to the limited spatial resolution in the vertical direction predicted by linear imaging theory. The magnitude of the artifacts decreased when smaller focal numbers were used, and also depended on properties of the imaging target (i.e., speed of sound contrast and radius). Typical reconstruction MAEs when using 2-D DBIM and slicing obtained in this work were above 25%, and overshoot artifacts as high as 50% above the intended speed of sound values were observed. In comparison, when using 3-D DBIM no artifacts or excessive blurring were observed when the transducers were properly distributed. A uniform distribution of point-like transducers over a spherical surface provided good results in terms of the reconstruction MAE values, which were around 13% for the analyzed imaging targets. Simulation results suggest that similar results in terms of the reconstruction error can be obtained if the transducers are arranged on a cylindrical surface. The cylinder array configuration may allow for easier imaging target placement when compared to the sphere array. Even further, it was observed that introducing an angular shift between adjacent rings can dramatically improve the image quality obtained with this array configuration. The use of angular shifting was found to reduce the reconstruction error by factors as large as 2.8 when compared to the simple cylinder array with transducers arranged in columns.

## Acknowledgment

The authors would like to thank Dr. S. Bond, Dr. J. Jin, Dr. W. D. O'Brien, Jr., and M. Milla for many helpful suggestions and discussions throughout the present work.

## REFERENCES


[1] J. Greenleaf, S. Johnson, S. Lee, G. Herman, and E. Wood, "Algebraic reconstruction of spatial distributions of acoustic absorption within tissue from their two-dimensional acoustic projections," *Acoust. Holography*, vol. 5, pp. 591–603, 1974.

[2] J. Greenleaf, S. Johnson, W. Samayoa, and F. Duck, "Algebraic reconstruction of spatial distributions of acoustic velocities in tissue from their time-of-flight profiles," *Acoust.Holography*, vol. 6, pp. 71–90, 1975.

[3] S. Norton, "Reconstruction of a two-dimensional reflecting medium over a circular domain: Exact solution," *J. Acoust. Soc. Am.*, vol. 67, no. 4, pp. 1266–1273, Apr. 1980.

[4] A. Devaney, "A filtered backpropagation algorithm for diffraction tomography," *Ultrason. Imag.*, vol. 4, no. 4, pp. 336–350, Oct. 1982.

[5] S. Norton and M. Linzer, "Correcting for ray refraction in velocity and attenuation tomography: A perturbation approach," *Ultrason. Imag.*, vol. 4, no. 3, pp. 201–233, Jul. 1982.

[6] F. Natterer and F. Wubbeling, "A propagation-backpropagation method for ultrasound tomography," *Inverse Problems*, vol. 11, no. 6, pp. 1225–1232, Dec. 1995.

[7] T. D. Mast, A. I. Nachman, and R. C. Waag, "Focusing and imaging using eigenfunctions of the scattering operator," *J. Acoust. Soc. Am.*, vol. 102, no. 2, pp. 715–725, Aug. 1997.

[8] P. M. van den Berg and R. E. Kleinman, "A contrast source inversion method," *Inverse Problems*, vol. 13, no. 6, pp. 1607–1620, Dec. 1997.

[9] W. C. Chew and Y. M. Wang, "Reconstruction of two-dimensional permittivity distribution using the distorted Born iterative method," *IEEE Trans. Med. Imag.*, vol. 9, no. 2, pp. 218–225, Jun. 1990.

[10] D. Borup, S. Johnson, W. Kim, and M. Berggren, "Nonperturbative diffraction tomography via Gauss-Newton iteration applied to the scattering integral equation," *Ultrason. Imag.*, vol. 14, no. 1, pp. 69–85, Jan. 1992.

[11] W. C. Chew and J. H. Lin, "A frequency-hopping approach for microwave imaging of large inhomogeneous bodies," *IEEE Microwave Guided Wave Lett.*, vol. 5, no. 12, pp. 440–441, Dec. 1995.

[12] O. Haddadin and E. Ebbini, "Imaging strongly scattering media using a multiple frequency distorted Born iterative method," *IEEE Trans. Ultrason., Ferroelectr., Freq. Control*, vol. 45, no. 6, pp. 1485–1496, Nov. 1998.

[13] P. Lasaygues, R. Guillermin, and J. P. Lefebvre, "Distorted Born diffraction tomography applied to inverting ultrasonic field scattered by noncircular infinite elastic tube," *Ultrason. Imag.*, vol. 28, no. 4, pp. 211–229, Oct. 2006.

[14] R. J. Lavarello and M. L. Oelze, "A study on the reconstruction of moderate contrast targets using the distorted Born iterative method," *IEEE Trans. Ultrason., Ferroelectr., Freq. Control*, vol. 55, no. 1, pp. 112–124, Jan. 2008.

[15] M. P. Andre, H. S. Janee, P. J. Martin, G. P. Otto, B. A. Spivey, and D. A. Palmer, "High-speed data acquisition in a diffraction tomography system employing large-scale toroidal arrays," *Int. J. Imag. Syst. Technol.*, vol. 8, no. 1, pp. 137–147, 1997.

[16] R. C. Waag and R. J. Fedewa, "A ring transducer system for medical ultrasound research," *IEEE Trans. Ultrason., Ferroelectr., Freq. Control*, vol. 53, no. 10, pp. 1707–1718, Oct. 2006.

[17] F. Simonetti, L. Huang, N. Duric, and O. Rama, "Super-resolution ultrasound tomography: A preliminary study with a ring array," in *Proc. SPIE*, 2007, vol. 6510, pp. 65 103F1–65 103F7.

[18] J. Wiskin, D. Borup, S. Johnson, M. Berggren, T. Abbott, and R. Hanover, "Full wave, non-linear, inverse scattering," *Acoust. Imag.*, vol. 28, pp. 183–194, 2007.

[19] H. Gemmeke and N. V. Ruiter, "3-D ultrasound computer tomography for medical imaging," *Nucl. Instrum. Methods Phys. Res. A*, vol. 580, no. 2, pp. 1057–1065, Oct. 2007.

[20] S. Y. Semenov, R. H. Svenson, A. E. Bulyshev, A. E. Souvorov, A. G. Nazarov, Y. E. Sizov, V. G. Posukh, A. Pavlovsky, P. N. Repin, A. N. Starostin, B. A. Voinov, M. Taran, G. P. Tatsis, and V. Y. Baranov, "Three-dimensional microwave tomography: Initial experimental imaging of animals," *IEEE Trans. Biomed. Eng.*, vol. 49, no. 1, pp. 55–63, Jan. 2002.

[21] F. Li, Q. H. Liu, and L. P. Song, "Three-dimensional reconstruction of objects buried in layered media using Born and distorted Born iterative methods," *IEEE Geosci. Remote Sens. Lett.*, vol. 1, no. 2, pp. 107–111, Apr. 2004.

[22] J. de Zaeytijd, A. Franchois, C. Eyraud, and J.-M. Geffrin, "Full-wave three-dimensional microwave imaging with a regularized Gauss-Newton method—Theory and experiment," *IEEE Trans. Antennas Propagat.*, vol. 55, no. 11, pp. 3279–3292, Nov. 2007.

[23] J. H. Lin and W. C. Chew, "Three-dimensional microwave imaging by local shape function method with CGFFT," in *IEEE Antennas Propagat. Soc. Int. Symp.*, 1996, vol. 3, pp. 2148–2151.

[24] M. Vogeler, "Reconstruction of the three-dimensional refractive index in electromagnetic scattering by using a propagation-backpropagation method," *Inverse Problems*, vol. 19, no. 3, pp. 739–753, Jun. 2003.

[25] K. Belkebir, P. C. Chaumet, and A. Sentenac, "Influence of multiple scattering on three-dimensional imaging with optical diffraction tomography," *J. Opt. Soc. Am.*, vol. 23, no. 3, pp. 586–595, Mar. 2006.

[26] K. W. A. van Dongen and W. M. D. Wright, "A full vectorial contrast source inversion scheme for three-dimensional acoustic imaging of both compressibility and density profiles," *J. Acoust. Soc. Am.*, vol. 121, no. 3, pp. 1538–1549, Mar. 2007.

[27] J.-M. Geffrin, P. C. Chaumet, C. Eyraud, K. Belkebir, and P. Sabouroux, "Electromagnetic three-dimensional reconstruction of targets from free space experimental data," *App. Phys. Lett.*, vol. 92, no. 19, pp. 194103-1–194103-3, May 2008.

[28] T. Hohage, "On the numerical solution of a three-dimensional inverse medium scattering problem," *Inverse Problems*, vol. 17, no. 6, pp. 1743–1763, Dec. 2001.

[29] N. V. Alekseenko, V. A. Burov, and O. D. Rumyantseva, "Solution of the three-dimensional inverse acoustic scattering problem on the basis of the Novikov-Henkin algorithm," *Acoust. Phys.*, vol. 51, no. 4, pp. 367–375, Aug. 2005.

[30] O. R. Halse, J. J. Stamnes, and A. J. Devaney, "Three-dimensional diffraction tomography by two-dimensional sectioning," *Opt. Commun.*, vol. 224, no. 6, pp. 185–195, Sep. 2003.

[31] Z. Q. Zhang and Q. H. Liu, "Three-dimensional nonlinear image reconstruction for microwave biomedical imaging," *IEEE Trans. Biomed. Eng.*, vol. 51, no. 3, pp. 544–548, Mar. 2004.

[32] M. Tracy and S. Johnson, "Inverse scattering solutions by a sine basis, multiple source, moment method—Part II: Numerical evaluations," *Ultrason. Imag.*, vol. 5, no. 4, pp. 376–392, Oct. 1983.

[33] R. J. Lavarello and M. L. Oelze, "Density imaging using inverse scattering," *J. Acoust. Soc. Am.*, vol. 125, no. 2, pp. 793–802, Feb. 2009.

[34] T. Cavicchi, S. Johnson, and W. D. O'Brien, Jr., "Application of the sine basis moment method to the reconstruction of infinite circular cylinders," *IEEE Trans. Ultrason., Ferroelectr., Freq. Control*, vol. 35, no. 1, pp. 22–33, Jan. 1988.

[35] M. Slaney, A. Kak, and L. Larsen, "Limitations of imaging with first-order diffraction tomography," *IEEE Trans. Microwave Theory Tech.*, vol. 32, no. 8, pp. 860–874, Aug. 1984.

[36] F. G. Mitri, "Acoustic scattering of a high-order Bessel beam by an elastic sphere," *Ann. Phys.*, vol. 323, no. 11, pp. 2840–2850, Nov. 2008.

[37] K. B. Ocheltree and L. A. Frizzell, "Sound field calculation for rectangular sources," *IEEE Trans. Ultrason., Ferroelectr., Frequency Control*, vol. 36, no. 2, pp. 242–248, Mar. 1989.

[38] O. Sakai, Y. Shen, Y. Takata, and M. Furuse, "The use of deblurring technique for improving the longitudinal resolution in helical CT of the head and neck region," *Comput. Med. Imag. Graphics*, vol. 21, no. 3, pp. 153–164, May–Jun. 1997.

[39] G. Wang, M. W. Vannier, M. W. Skinner, M. G. R. Cavalcanti, and G. W. Harding, "Spiral CT image deblurring for cochlear implantation," *IEEE Trans. Med. Imag.*, vol. 17, no. 2, pp. 251–262, Apr. 1998.

[40] M. Mignotte and J. Meunier, "Three-dimensional blind deconvolution of SPECT images," *IEEE Trans. Biomed. Eng.*, vol. 47, no. 2, pp. 274–280, Feb. 2000.

[41] M. Jiang, G. Wang, M. W. Skinner, J. T. Rubinstein, and M. W. Vannier, "Blind deblurring of spiral CT images," *IEEE Trans. Med. Imag.*, vol. 22, no. 7, pp. 837–845, Jul. 2003.

[42] S. J. Norton and M. Linzer, "Ultrasonic reflectivity imaging in three dimensions: Exact inverse scattering solutions for plane, cylindrical, and spherical apertures," *IEEE Trans. Biomed. Eng.*, vol. 28, no. 2, pp. 202–220, Feb. 1981.

[43] E. B. Saff and A. B. J. Kuijlaars, "Distributing many points on a sphere," *Math. Intell.*, vol. 19, no. 1, pp. 5–14, 1997.

[44] T. Erber and G. M. Hockney, "Equilibrium configurations of N equal charges on a sphere," *J. Phys. A (Math. General)*, vol. 24, no. 23, pp. L1369–L1377, Dec. 1991.

[45] V. C. Anderson, "Sound scattering from a fluid sphere," *J. Acoust. Soc. Am.*, vol. 22, no. 4, pp. 426–631, Jul. 1950.

[46] R. C. Gonzalez and R. E. Woods, *Digital Image Processing*. Upper Saddle River, NJ: Prentice Hall, 2007.
[47] E. Wolf, "Three-dimensional structure determination of semi-transparent objects from holographic data," *Opt. Commun.*, vol. 1, no. 4, pp. 153–156, Sep./Oct. 1969.
[48] E. Wolf, A. Consortini, Ed., "Principles and development of diffraction tomography," in *Trends Optics*, 1996.
[49] M. Born and E. Wolf, *Principles of Optics*. Cambridge, U.K.: Cambridge Univ. Press, 2002.
[50] J. N. Yang, A. D. Murphy, E. L. Madsen, J. A. Zagzebski, K. W. Gilchrist, G. R. Frank, M. C. Macdonald, C. A. Millard, A. Faraggi, C. A. Jaramillo, and F. R. Gosset, "A method for in vitro mapping of ultrasonic speed and density in breast tissue," *Ultrason. Imag.*, vol. 13, no. 1, pp. 91–109, Jan. 1991.
[51] P. D. Edmons, C. L. Mortensen, J. R. Hill, S. K. Holland, J. F. Jensen, P. Schattner, A. D. Valdes, R. H. Lee, and F. A. Marzoni, "Ultrasound tissue characterization of breast biopsy specimens," *Ultrason. Imag.*, vol. 13, no. 2, pp. 162–185, Apr. 1991.
[52] S. A. Johnson, T. Abbott, R. Bell, M. Berggren, D. Borup, D. Robinson, J. Wiskin, S. Olsen, and B. Hanover, "Noninvasive breast tissue characterization using ultrasound speed and attenuation," *Acoust. Imag.*, vol. 28, pp. 147–154, 2007.
[53] C. Li, N. Duric, and L. Huang, "Clinical breast imaging using sound-speed reconstructions of ultrasound tomography data," in *Proc. SPIE*, 2008, vol. 6920, pp. 692009-1–692009-9.
[54] A. J. Hesford and W. C. Chew, "A frequency-domain formulation of the Frechet derivative to exploit the inherent parallelism of the distorted Born iterative method," *Waves Random Complex Media*, vol. 16, no. 4, pp. 495–508, Nov. 2006.
[55] D. L. Donoho, "Compressed sensing," *IEEE Trans. Inf. Theory*, vol. 52, no. 4, pp. 1289–1306, Apr. 2006.
[56] M. Lustig, D. Donoho, and J. M. Pauly, "Sparse MRI: The application of compressed sensing for rapid MR imaging," *Magn. Reson. Med.*, vol. 58, no. 6, pp. 1182–1195, Dec. 2007.
[57] J. Trzasko and A. Manduca, "Highly undersampled magnetic resonance image reconstruction via homotopic $l_0$-minimization," *IEEE Trans. Med. Imag.*, vol. 28, no. 1, pp. 106–121, Jan. 2009.
[58] J. Provost and F. Lesage, "The application of compressed sensing for photo-acoustic tomography," *IEEE Trans. Med. Imag.*, vol. 28, no. 4, pp. 585–594, Apr. 2009.
[59] C. Li, N. Duric, and L. Huang, "Breast imaging using transmission ultrasound: Reconstructing tissue parameters of sound speed and attenuation," in *Int. Conf. BioMedical Eng. Inf.*, 2008, vol. 2, pp. 708–712.
[60] A. Austeng and S. Holm, "Sparse 2-D arrays for 3-D phased array imaging—Design methods," *IEEE Trans. Ultrason., Ferroelectr., Freq. Control*, vol. 49, no. 8, pp. 1073–1086, Aug. 2002.